

Complex fault system revealed from 3-D seismic reflection data with deep learning and fault network analysis

Thilo Wrona^{1,2*}, Indranil Pan^{3,4,5}, Rebecca E. Bell⁶, Christopher A-L. Jackson⁷, Robert L. Gawthorpe¹, Haakon Fossen⁸, Edoseghe E. Osagiede¹, and Sascha Brune^{2,9}

¹Department of Earth Science, University of Bergen, Allégaten 41, N-5007 Bergen, Norway.

²GFZ German Research Centre for Geosciences, Telegrafenberg, 14473 Potsdam, Germany.

³Centre for Process Systems Engineering & Centre for Environmental Policy, Imperial College London, UK.

⁴The Alan Turing Institute, British Library, London, UK.

⁵School of Mathematics, Statistics & Physics, Newcastle University, UK.

⁶Basins Research Group (BRG), Department of Earth Science and Engineering, Imperial College, Prince Consort Road, London, SW7 2BP, UK.

⁷Department of Earth and Environmental Sciences, University of Manchester, Manchester, UK

⁸Museum of Natural History, University of Bergen, Allégaten 41, N-5007 Bergen, Norway.

⁹Institute of Geosciences, University of Potsdam, Potsdam-Golm, Germany.

*wrona@gfz-potsdam.de

ABSTRACT

Understanding where normal faults are is critical to an accurate assessment of seismic hazard, the successful exploration for and production of natural (including low-carbon) resources, and for the safe subsurface storage of CO₂. Our current knowledge of normal fault systems is largely derived from seismic reflection data imaging intra-continental rifts and continental margins. However, exploitation of these data is limited by interpretation biases, data coverage and resolution, restricting our understanding of fault systems. Applying supervised deep learning to one of the largest offshore 3-D seismic reflection data sets from the northern North Sea allows us to image the complexity of the rift-related fault system. The derived fault score volume allows us to extract almost 8000 individual normal faults of different geometries, which together form an intricate network characterised by a multitude of splays, junctions and intersections. Combining tools from deep learning, computer vision and network analysis allows us to map and analyse the fault system in great detail and a fraction of the time required by conventional interpretation methods. As such, this study shows how we can efficiently identify and analyse fault systems in increasingly large 3-D seismic data sets.

37

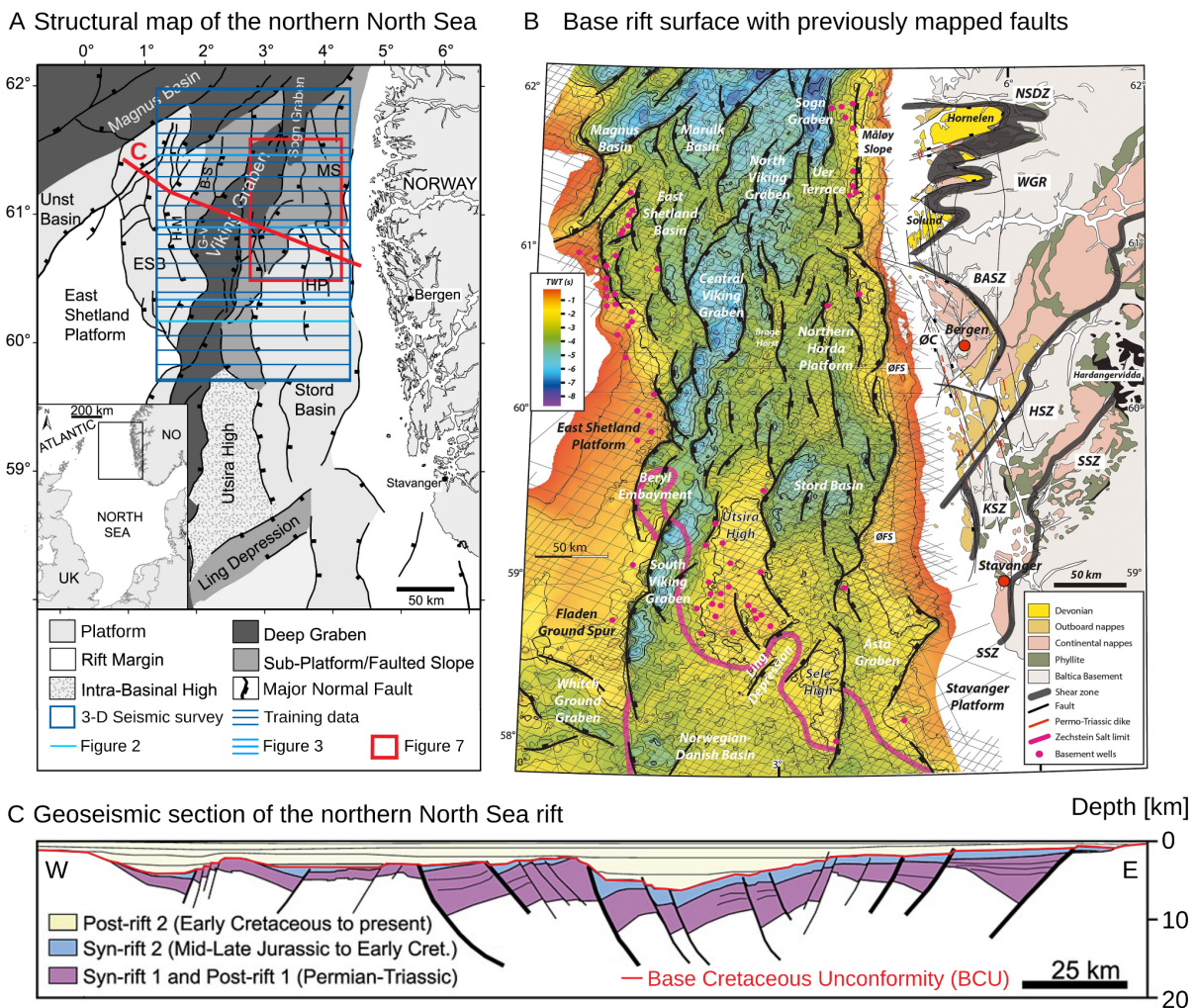
38 1. INTRODUCTION

39 Understanding the geometry and growth of normal fault systems is critical when assessing
40 seismic hazard, when identifying suitable sites for subsurface CO₂ storage and when exploring for
41 natural resources (traditional and low-carbon). For example, whereas probabilistic seismic hazard
42 analyses based on seismic event catalogues are extremely useful when trying to forecast earthquake
43 likelihood and location, high-resolution fault mapping, preferably in 3-D, can help us constrain the
44 slip tendency of faults, where seismic catalogues are discontinuous and/or incomplete (e.g. Morris et
45 al., 1996; Moeck et al., 2009; Yukutake et al., 2015). Moreover, faults can facilitate (or impede) fluid
46 and gas migration to the Earth's surface, thus determining their geometry and connectivity, as well as
47 their hydraulic properties is key for assessing their role in the long-term subsurface storage of CO₂
48 (Bissell et al., 2011; Kampman et al., 2014). In both of these examples, we need robust predictions of
49 3-D fault geometry over large areas and across a wide range of scales (100s m to 100 km).

50 Accurately mapping fault systems in 2-D and 3-D seismic reflection data typically requires
51 expertise and time (e.g. Bond, 2015). While we can map fault systems in great detail over small areas
52 using 3-D seismic reflection data (e.g. Lohr et al., 2008; Wrona et al., 2017; Claringbould et al.,
53 2020), we lack an understanding of the character of 3-D fault populations at the scale of entire rift
54 systems, as regional studies are often limited to only sparse, 2-D seismic sections (e.g. Clerc et al.,
55 2015; Fazlikhani et al., 2017; Phillips et al., 2019). 3-D numerical models are now capable of
56 simulating fault networks at the rift scale; however, there are few observational data sets of the same
57 scale to test the predictions of these models and, therefore, help refine them (e.g. Naliboff et al., 2020;
58 Pan et al., 2021).

59 Supervised deep learning allows us to map faults in seismic reflection data (e.g. Wu et al.,
60 2019; Mosser et al., 2020; Wrona et al., 2021a), but up until now many of these studies have laid the
61 foundation by been in the “proof of concept” phase, simply focusing on detecting faults rather than
62 studying ; such studies often have yet to provide new insights into the geometry of these normal
63 faults. In this study, by applying supervised deep learning to newly-acquired broadband 3-D seismic
64 reflection data imaging much of the northern North Sea rift (161 km wide in E-W, 266 km long area

65 in N-S, 0-20 km deep), we map the fault network associated with a continental rift basin at an
 66 unprecedented level of detail. Using manually labelled data (<0.1% of data volume), we train a deep
 67 convolutional neural network (U-Net) to predict faults in our data set. The predicted score ranges
 68 from 0 (no fault) to 1 (fault). Based on this score across the entire 3-D seismic volume we employ a
 69 second workflow to extract the normal fault system as a network (a set of nodes and edges) allowing
 70 us to investigate the architecture and growth of this extremely complex system consisting of
 71 thousands of intersecting faults.



72
 73 **Figure 1:** **A** Structural overview map of the northern North Sea basin system (from Tillmans et al.,
 74 2021 after Færseth, 1996). Blue rectangle marks the outline of the seismic survey in this study. ESB =
 75 East Shetland Basin, B-S = Brent-Statfjord Fault, G-V = Gullfaks-Visund Fault, MS = Måløy Slope,
 76 HP = Horda Platform. **B** The base rift surface (base Permo-Triassic rifting) time-structure map in the
 77 northern North Sea rift (from Fazlikhani et al., 2017) and the geology of southwestern Norway,
 78 showing the general onshore and offshore structural configuration in the study area. Bold black lines
 79 highlight major rift-related normal faults displacing the base rift surface where all units older than
 80 Upper Permian are considered basement. Black lines in the background show some of the 2-D seismic
 81 reflection surveys used by Fazlikhani et al. (2017). NSDZ, Nordfjord-Sogn Detachment Zone; BASZ,
 82 Bergen Arc Shear Zone; WGR, Western Gneiss Region; ØC, Øygarden Complex (gneiss); ØFS,

83 Øygarden Fault System; HSZ, KSZ, and; SSZ: Hardangerfjord, Karmøy, and Stavanger shear zones,
84 respectively. C Regional interpretation of the structure of the northern North Sea after Færseth (1996).

85 2. GEOLOGICAL SETTING

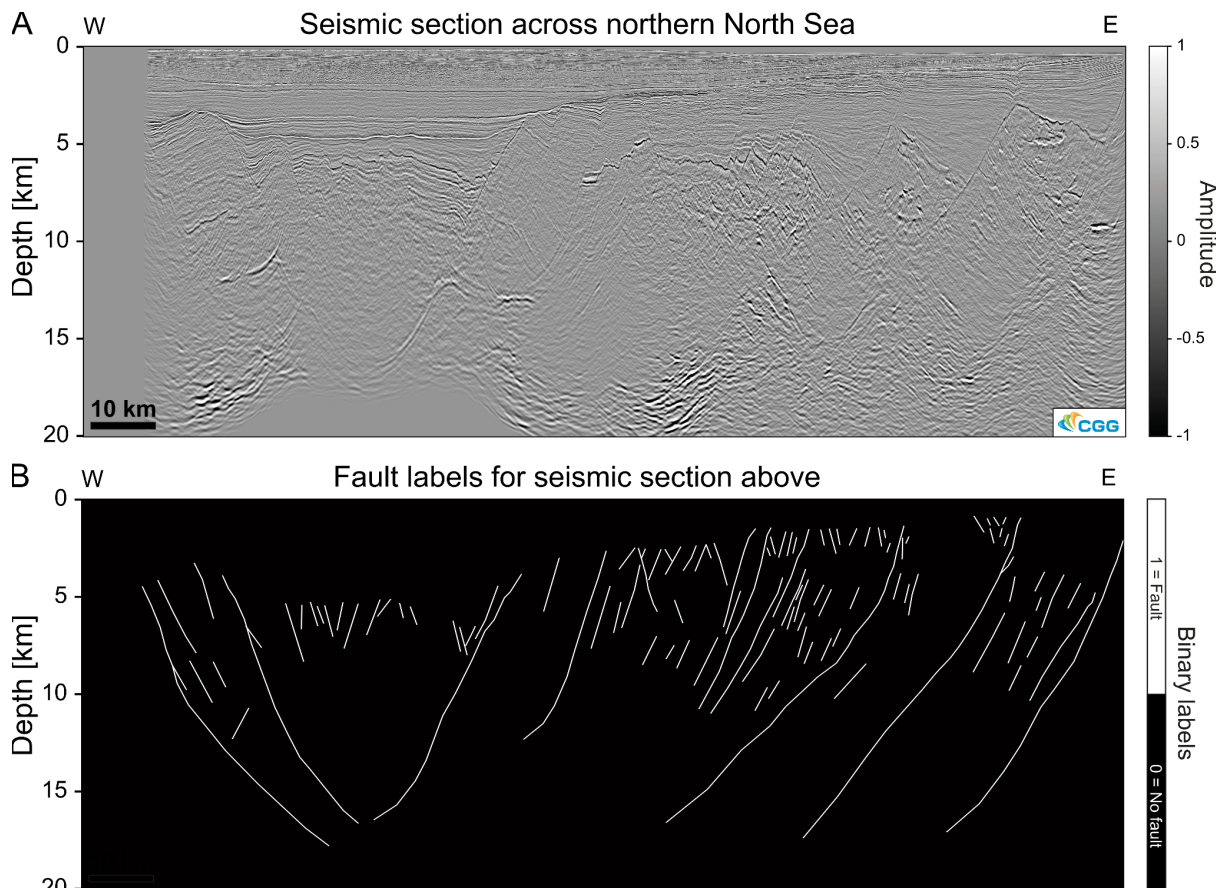
86 The study area is located in the northern North Sea (Fig. 1), where continental crust consists of
87 10–30-km-thick crystalline basement overlain by as much as 12 km of sedimentary strata deposited
88 during, after, and possibly even before periods of rifting in the late Permian–Early Triassic (rift phase
89 1) and Middle Jurassic–Early Cretaceous (rift phase 2) (e.g. Whipp et al., 2014; Bell et al., 2014;
90 Maystrenko et al., 2017). The extension direction of these two phases has long been debated. Whereas
91 most studies agree that the late Permian–Early Triassic rifting was driven by E-W extension (e.g.
92 Færseth et al., 1997; Torsvik et al., 1997), Middle Jurassic–Early Cretaceous rifting has been
93 associated with both E-W (e.g. Bartholomew et al., 1993; Brun and Tron, 1993) and NW-SE
94 extension (e.g. Færseth, 1996; Doré et al., 1997; Færseth et al., 1997) (Fig. 1B). This debate is further
95 complicated by the fact that some of the largest normal faults on the Horda Platform developed during
96 rift phase 1, but were subsequently reactivated during rift phase 2 (e.g. Whipp et al., 2014; Bell et al.,
97 2014). The crystalline basement underlying the sedimentary strata formed by terrane accretion during
98 the Sveconorwegian (1140–900 Ma) and Caledonian (460–400 Ma) orogenies (Bingen et al., 2008).
99 Several studies argue that this structural template, in particular the ductile shear zones, controlled the
100 location, strike, and overall pattern of rift-related faulting in the overlying sedimentary successions
101 being reactivated as normal faults, or by limiting the along-strike propagation of faults (e.g.
102 Fazlikhani et al., 2017; Phillips et al., 2019; Osagiede et al., 2020; Wiest et al., 2020).

103 3. DATA & METHODS

104 3.1. 3-D seismic reflection data

105 In this study, we use one of the largest offshore 3-D seismic data sets ever acquired, which
106 images a large part of the northern North Sea rift across an area of 35,410 km², and with excellent
107 depth-imaging down to 22 km (i.e., the middle-to-lower crust) (Figs. 1, 2A, 3). The data set was
108 acquired using eight, up to 8-km-long streamers that were towed ~40 m below the water surface. The
109 broadseis technology used for recording covers a wide range of frequencies (2.5-155 Hz), providing
110 high-resolution depth imaging. The data were binned at 12.5 × 18.75 m, with a vertical sample rate of

111 4 ms. The data was 3-D true amplitude prestack depth-migrated. The seismic volume was zero-phase
112 processed with SEG normal polarity; i.e., a positive reflection (white) corresponds to an acoustic
113 impedance (density \times velocity) increase with depth. More details on data acquisition and pre-
114 processing steps are provided by Wrona et al., (2019, 2021a).

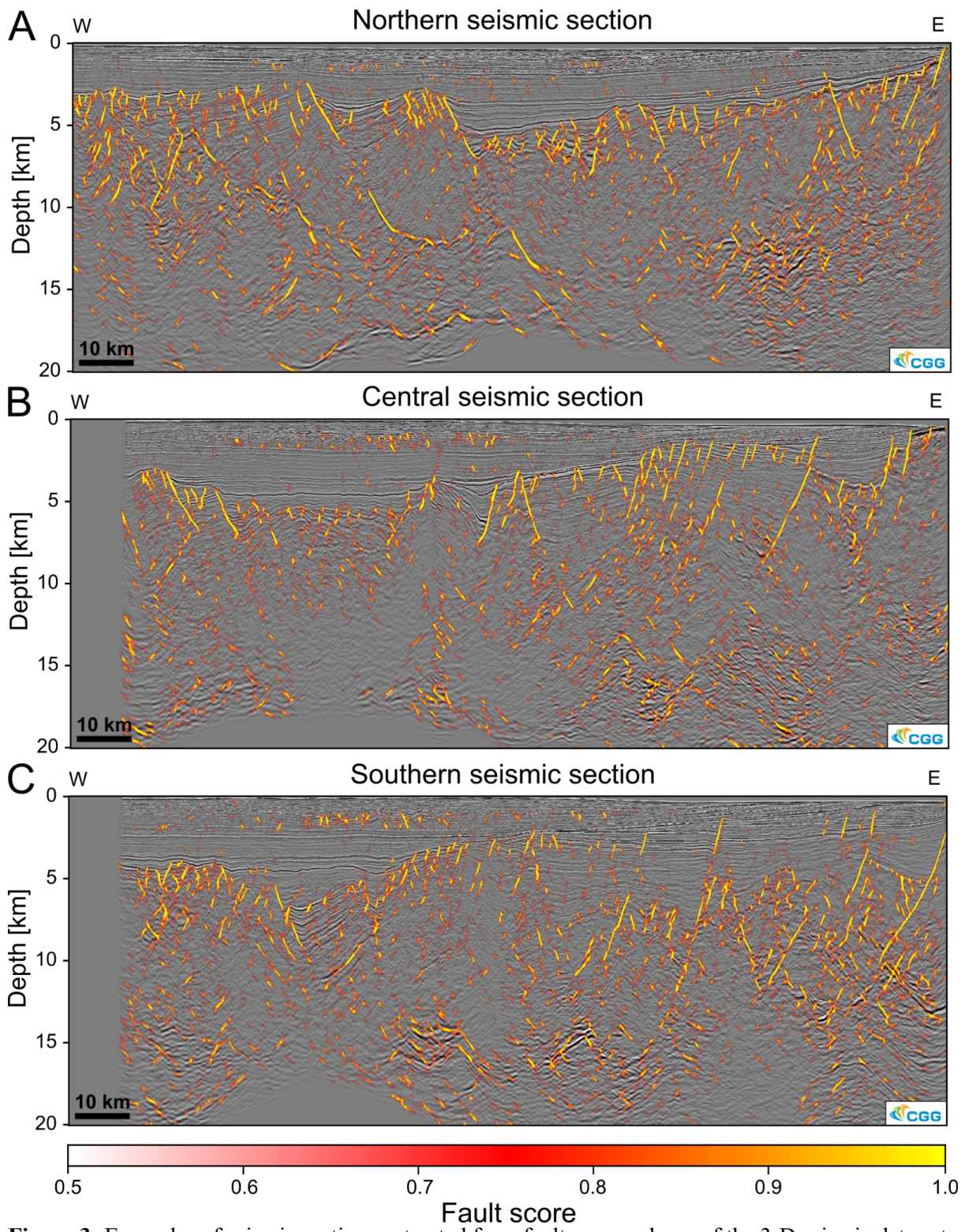


115 **Figure 2:** **A** Example seismic section across the northern North Sea. Amplitudes are scaled for
116 machine learning **B** Example of fault interpretation of the section used to train a deep convolutional
117 neural network for fault prediction.
118

119 3.2. Deep learning

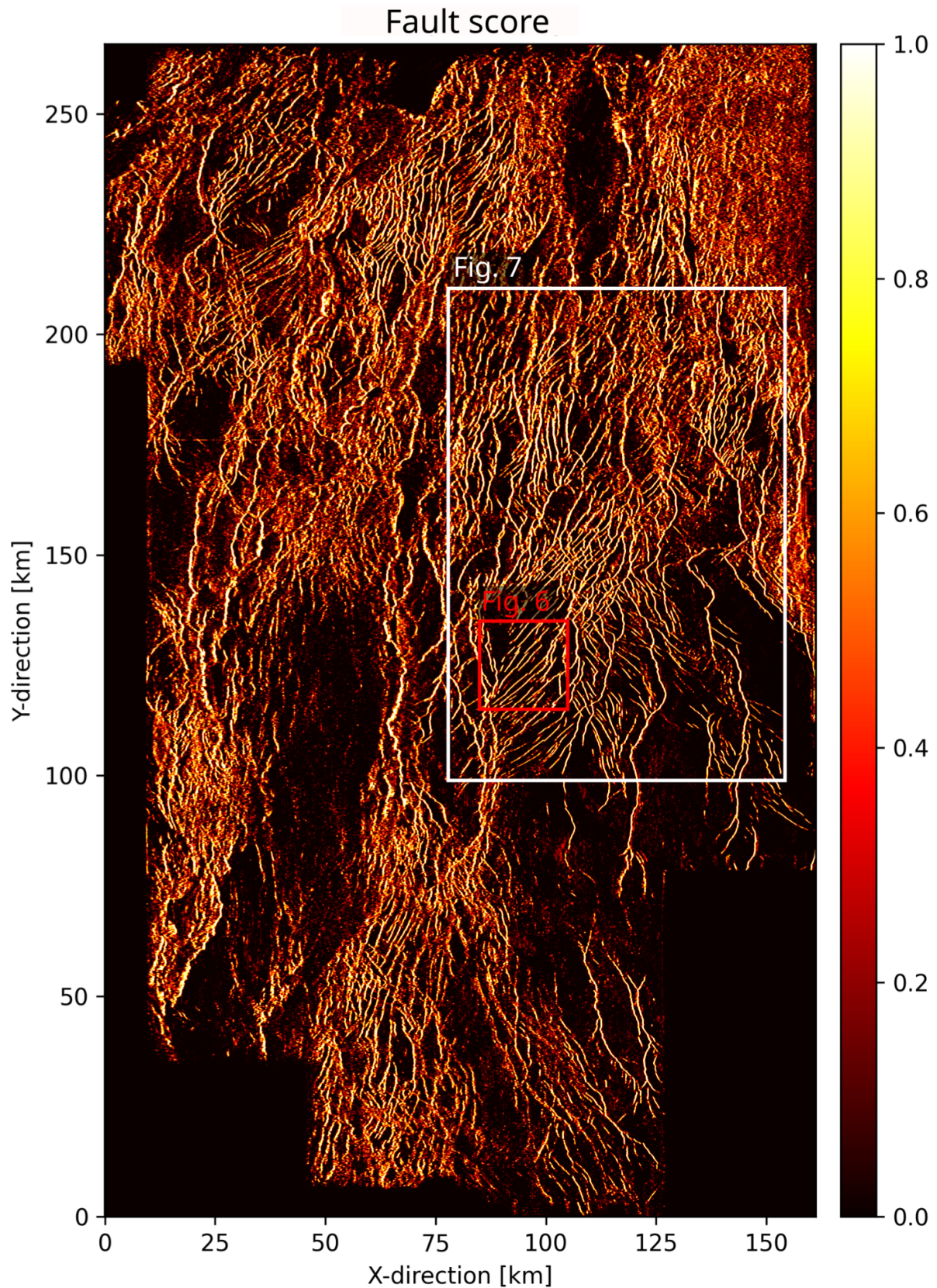
120 Deep learning describes a set of algorithms and models, which learn to perform a specific task
121 (e.g. fault interpretation) on a given data set without explicit feature engineering (e.g. the calculation
122 and calibration of seismic attributes, such as coherence or variance). Deep learning allows the
123 derivation of a fault score volume that highlights normal faults within a 3-D seismic volume. This
124 approach requires that a large number of examples of faults and unfaulted strata are labelled in the
125 training seismic data. We extract 80,000 such examples (2-D squares of 128 \times 128 pixels) from 22
126 interpreted seismic sections oriented perpendicular to the N-trending rift (Figs. 1A, 2). Note that these

127 seismic sections only constitute <0.1% of the entire 3-D seismic volume. Next, we split these
128 examples into three groups; one set for training (80%), one for validation (10%), and one for testing
129 (10%). We use the first of these to train a deep convolutional neural network (U-Net) designed to
130 perform image segmentation tasks (Ronneberger et al., 2015). Using the validation set, we track the
131 accuracy and loss of the model during training and stop once the validation loss does not decrease
132 further. Finally, we apply the model to the entire 3-D seismic volume to derive a fault score volume
133 (Figs. 3, 4), an attribute, which ranges from 0 (no fault) to 1 (fault). All details of the workflow and
134 the code are provided by Wrona et al. (2021b, 2021a).



135
 136
 137
 138
 139

Figure 3: Examples of seismic sections extracted from fault score volume of the 3-D seismic data set. Note that these sections were not part of the training data, but are actually 6.25 km away from the closest interpreted seismic section (see Fig. 1A).



140
 141 **Figure 4:** Surface capturing tectonic faults extracted from fault likelihood volume. The surface was
 142 extracted 500 m below the Base Cretaceous Unconformity, where we observe a large number of
 143 faults, which were either formed or reactivated in the second rift phase. White rectangle shows the
 144 area used for validation (Fig. 8) and the red rectangle indicates the area where we demonstrate our
 145 fault network extraction workflow (Fig. 6).

146
147
148
149
150

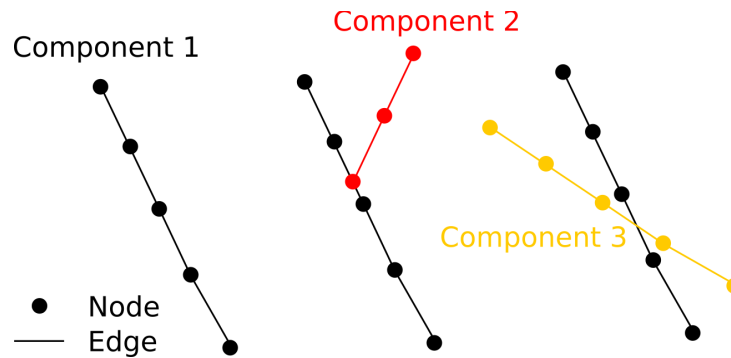
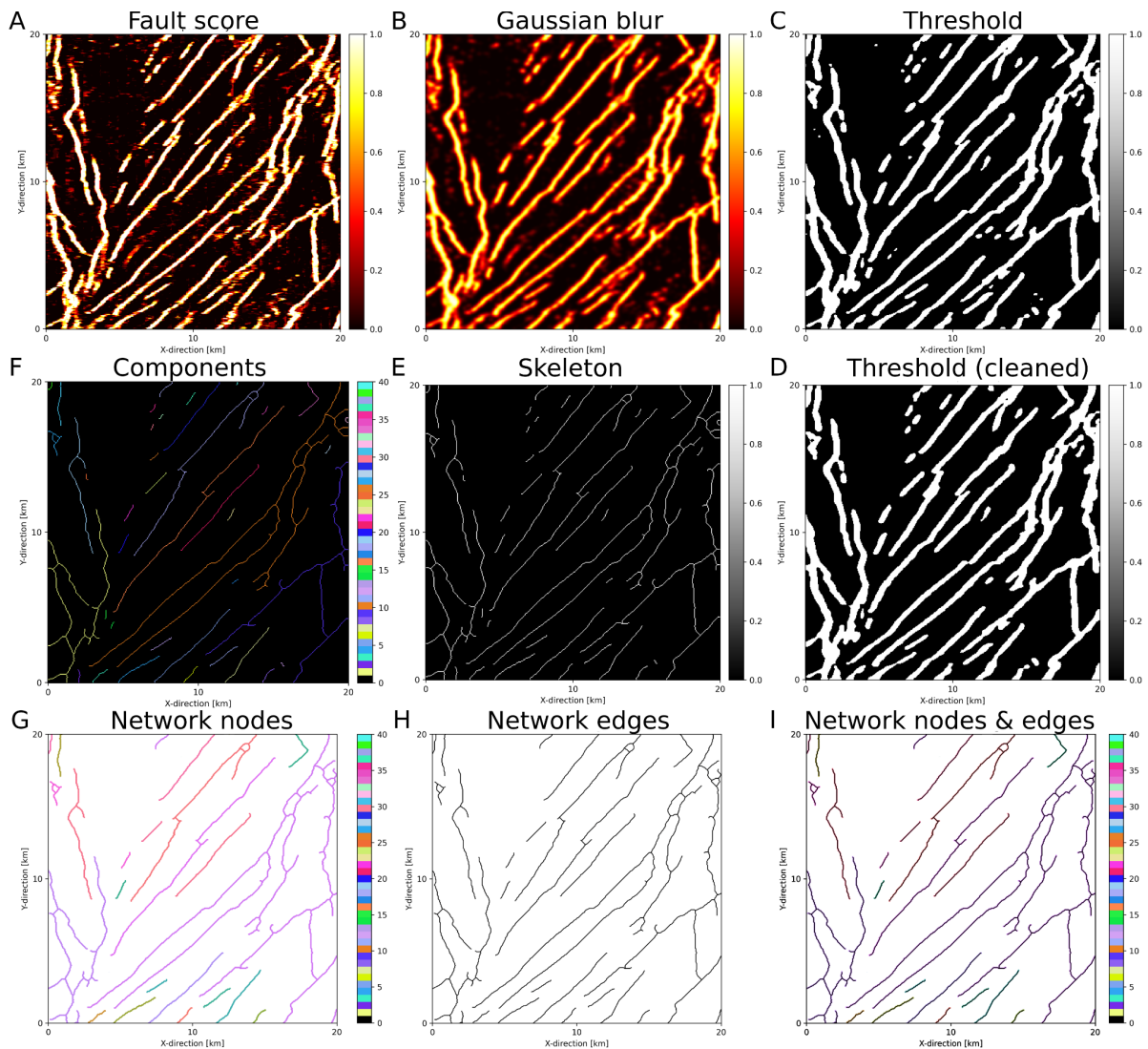


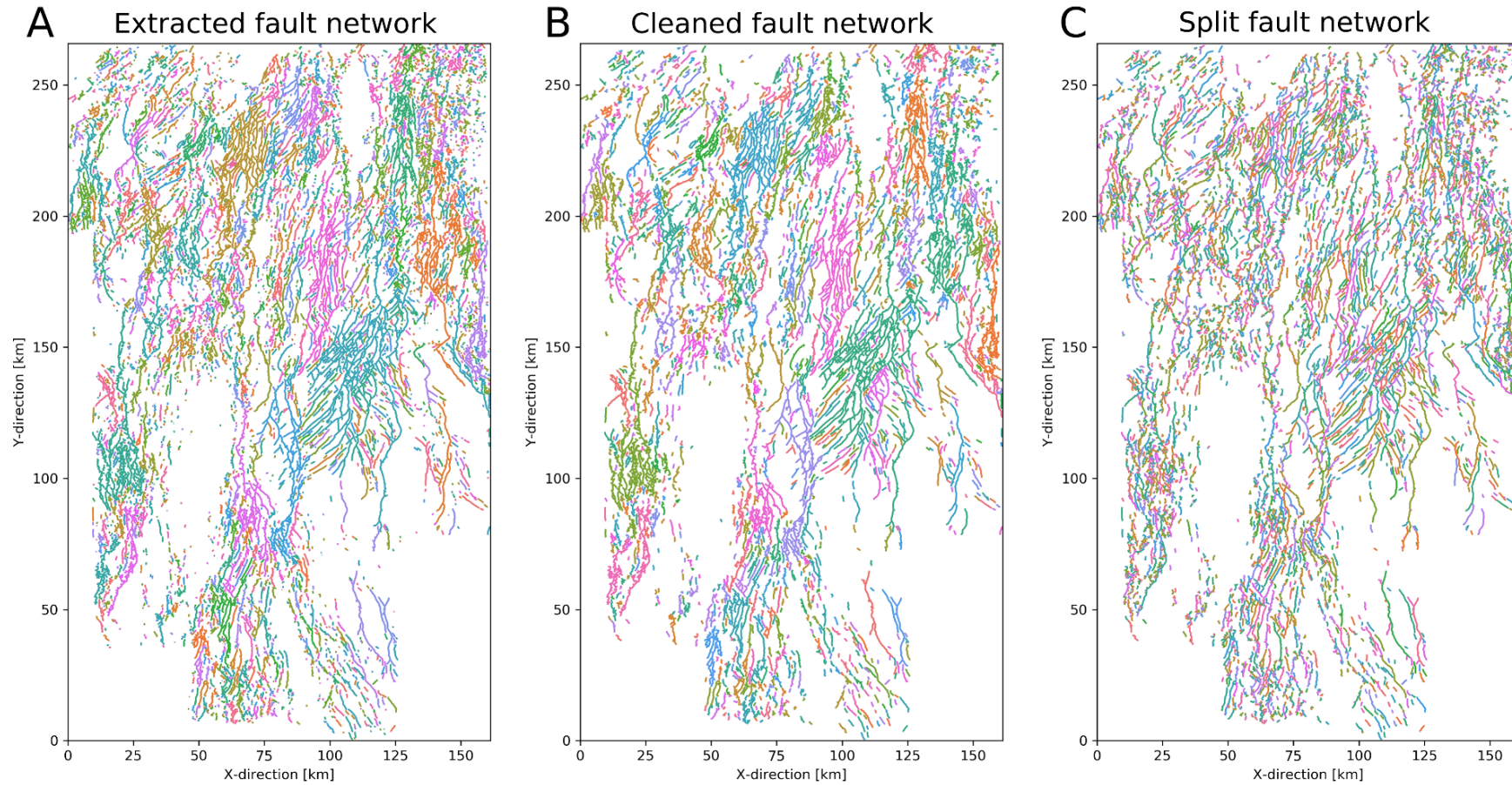
Figure 5: Schematic illustration of fault network (or graph) with nodes, edges and components. Each node marks a location along the fault. Each edge connects two nodes and each (connected) component indicates all nodes connected to one another by edges.



151
152
153
154
155
156
157

Figure 6: Fault network extraction workflow showing: **A** Fault score extracted along the surface (500 m below BCU). **B** Gaussian Blur filter ($\sigma=2$) of surface. **C** Threshold (0.35) of filter. **D** Cleaned threshold where small patches are removed. **E** Skeleton of cleaned threshold. **F** Connected components of skeleton. **G** Network nodes based on components. **H** Network edges based on components. **I** Network nodes and edges combined. Note that colours in F, G and I indicate connected components (i.e. individual faults), before splitting (see Fig. 6).

Fault network editing



158

159 **Figure 7:** **A** Fault network extracted from BCU (Fig. 4D). Note the large areas with the same colours resulting from multiple faults being grouped into one
160 connected component **B** Fault network after removal of noise (i.e. small components). **C** Fault network after splitting junctions previously connecting
161 splaying and intersecting faults. Note that large connected components are split up and individual faults are highlighted by different colours.

162 3.3. Automated fault network extraction and analysis

163 Extracting a fault network from the 3-D volume allows us to perform a comprehensive
164 geometric analysis of the fault system using our fault analysis toolbox - fatbox (Wrona et al., 2022).
165 The basic idea is to describe a fault system in 2-D as a network (or graph), i.e. sets of nodes and edges
166 (Fig. 5). Each node marks a location along the fault and each edge connects two nodes. All nodes
167 connected to one another by edges are labelled as a (connected) component.

168 Our fault extraction workflow consists of these eight steps: (1) extract horizon, (2) Gaussian
169 blur filter, (3) thresholding, (4) cleaning, (5) skeletonization, (6) connect components, (7) add nodes
170 to graph, (8) add edges to graph and (9) split junctions. While applying it to our North Sea target
171 region, we first attempt to capture as many faults as possible by extracting the fault score along a
172 horizon 500 m below Base Cretaceous Unconformity (BCU) (Fig. 1C). Here we observe a large
173 number of faults, which were either formed in the second rift phase, or formed in the first rift phase
174 and reactivated in the second rift phase (Figs. 4, 6A). Second, we apply a Gaussian blur filter to
175 increase [lateral](#) fault continuity (Fig. 6B). Third, we apply a threshold of 0.35 to separate the faults
176 from the background in the fault likelihood (Fig. 6C). This threshold is a tradeoff, which balances
177 capturing as many faults as possible (lower values) and identifying clearly resolvable faults (high
178 values). Four, we further restrict this threshold and essentially filter these points by removing areas
179 smaller than 25 pixels (Fig. 6D). Five, we collapse the faults to one-pixel wide lines using
180 skeletonization (Guo and Hall, 1992) (Fig. 6E). Six, we label adjacent pixels in the image as
181 connected components (Wu et al., 2009) (Fig. 6F). Each component consists of pixels which are
182 connected to each other. These components represent the faults in the network. At this point, we can
183 build our graph using these connected components of the image (Fig. 6F). Each pixel belonging to a
184 component becomes a node whereas edges are created between neighbouring nodes (Fig 6G-I). This
185 process results in a number of faults with splays, junctions or intersections being grouped into one
186 connected component (Fig. 7A). To correct this, we split up junctions (nodes with three edges) based
187 on the similarity of strike, i.e. aligned branches remain connected (Fig. 7B,C). This final network is
188 compared to the Base Late Jurassic horizon mapped by Tillmans et al., (2021) (Fig. 8). Additionally,

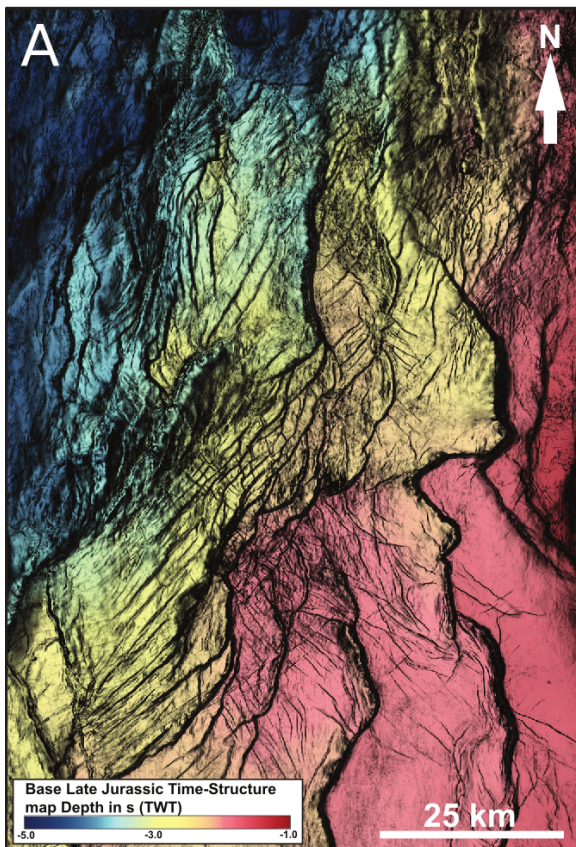
189 we perform the exact same workflow on ten slices through the fault score volume (1-10 km depth) to
190 capture 3-D fault geometries with depth (Fig. 9).

191 After extracting the fault system, we calculate a series of typical fault properties using our fault
192 analysis toolbox - fatbox (Wrona et al., 2022) (Fig. 10). First, we calculate the fault length as the sum
193 of the edge lengths of each component (Fig. 10B). Second, we calculate the strike along the fault from
194 neighbouring nodes (Fig. 10C). If we were to calculate the overall fault strike, we would overlook
195 along-strike variations in strike. If we were to calculate the strike as the orientation of each edge, we
196 would only obtain values of 0, 45 or 90°, because the nodes are closely spaced. Instead, we calculate
197 the strike from the 3rd degree neighbouring nodes (i.e. neighbours of neighbours of neighbours). This
198 assures a robust, high resolution fault strike calculation. Combining the fault length and strike, we can
199 generate a length-weighted Rose diagram (Fig. 10C). Finally, we calculate the fault density as the
200 fault length per area (Fig. 10D).

201 3.4. Comparison to conventional seismic interpretation

202 We can ask ourselves, “how good are our results compared to a state-of-the-art fault
203 interpretation from the same data set using conventional fault mapping techniques?” (Fig. 8). Tillmans
204 et al., (2021) map the Base Late Jurassic (base of syn-rift sediments associated with rift phase 2) on
205 the eastern flank of the North Viking Graben (see Figs. 1A, 4 for location) using a combination of
206 manual picking and auto-tracking [on the same seismic dataset](#). This horizon is calibrated with 40
207 exploration wells, which provide direct constraints on the depth of the surface. Tillmans et al. (2021)
208 highlight the fault system by computing the variance attribute (Chopra and Marfurt, 2007) along the
209 horizon (Fig. 7A). On top of the horizon, we plot the fault network mapped from the fault score
210 extracted 500 m below the easily-mappable Base Cretaceous Unconformity (BCU) (Fig. 8B). This
211 visual comparison shows that while we are missing a few faults in the southwest of the map, we are
212 able to identify and accurately represent most of the faults identified by Tillmans et al. (2021). The
213 missing faults are either overlooked by our model (i.e. false negatives) or result from the difference in
214 the horizons that we compare: Base Cretaceous Unconformity (our study) versus Base Late Jurassic
215 (Tillmans et al., 2021).

Time-structure map



+ extracted fault network

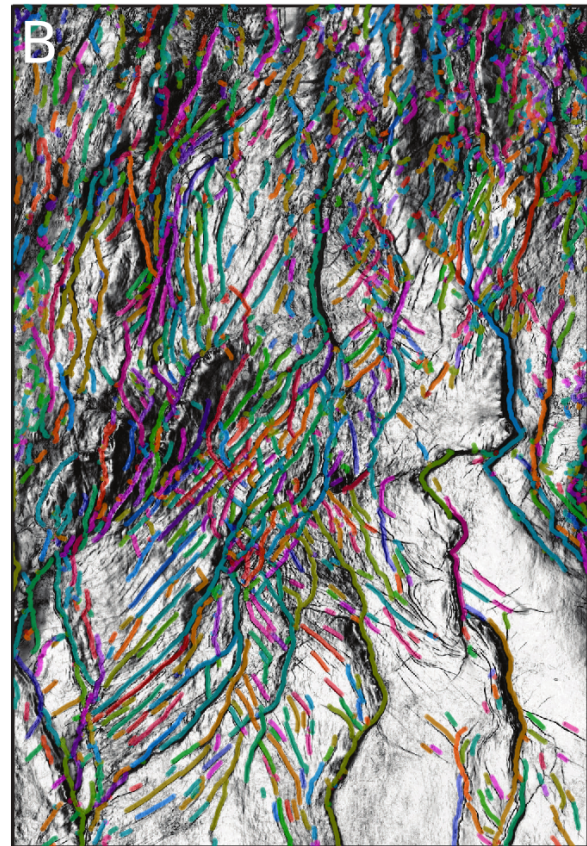
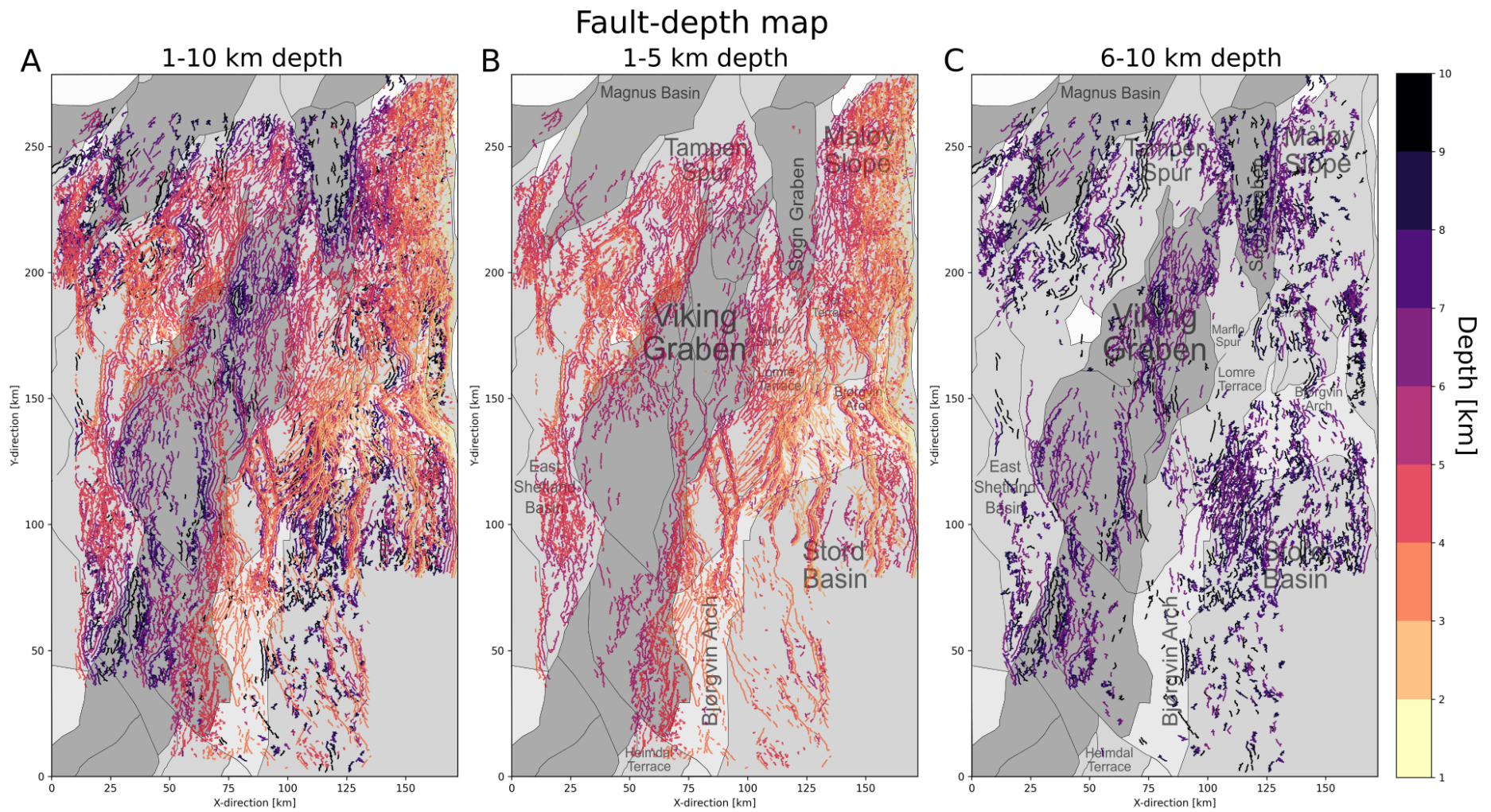
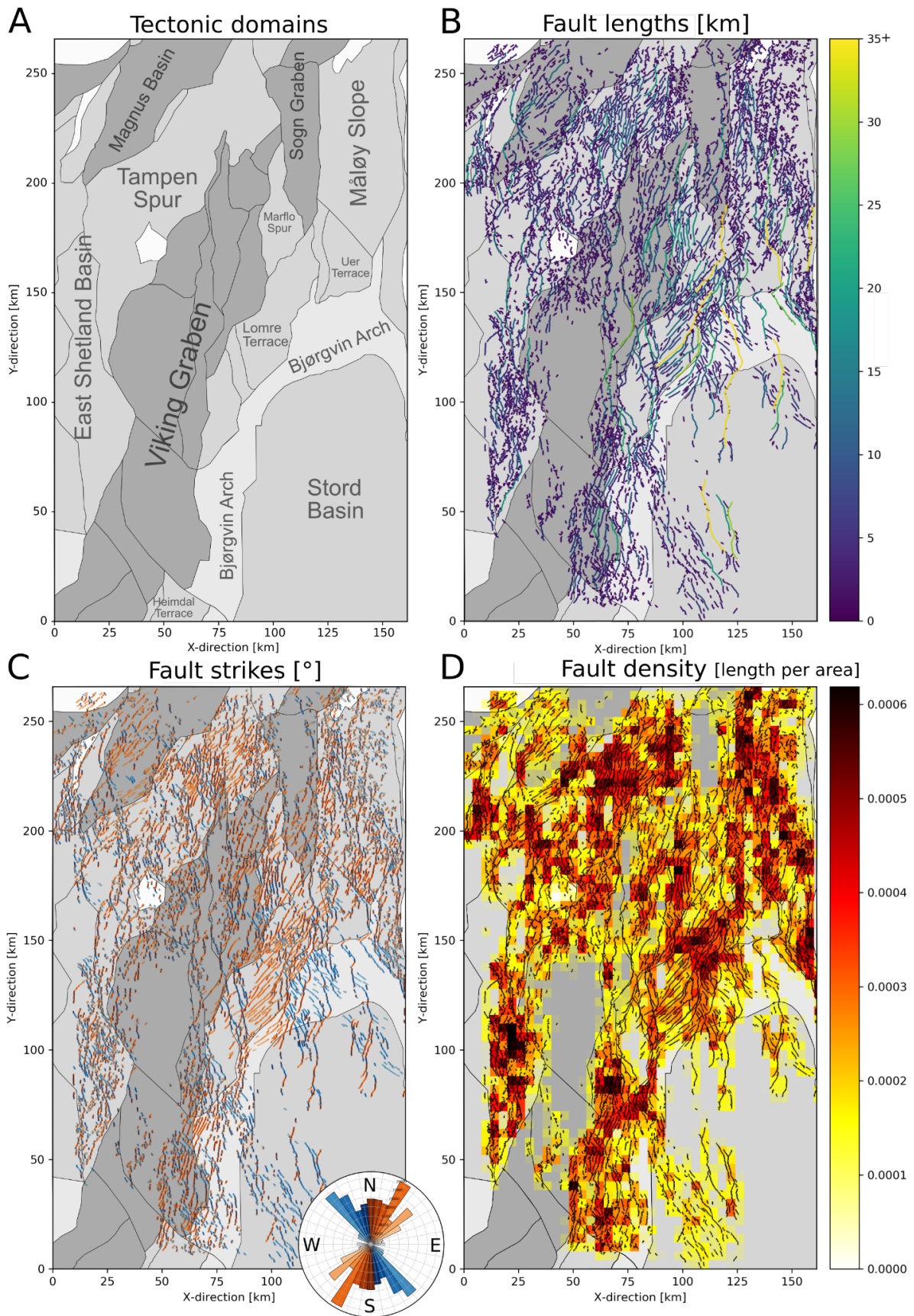
217
218
219
220

Figure 8: Comparison of **A** Base Late Jurassic time-structure map interpreted by Tillmans et al., (2021) and **B** Automatically-extracted fault network 500 m below Base Cretaceous Unconformity, using the same seismic dataset. Faults are distinguished by colour.



221
222
223

Figure 9: Fault map of the northern North Sea extracted every kilometre between 1-10 km depth (A), 1-5 km depth (B) and 6-10 km depth (C) with structural elements from the Norwegian Petroleum Directorate or NPD (2022).



224
225
226
227

Figure 10: **A** Structural elements of the northern North Sea Rift (NPD, 2022) **B** Fault lengths (500 m below BCU) on top of structural elements. **C** Fault strikes (500 m below BCU) on top of structural elements with length-weighted Rose diagram. **D** Fault density on top of structural elements.

228
229
230
231
232
233
234
235
236
237
238
239
240
241
242
243
244

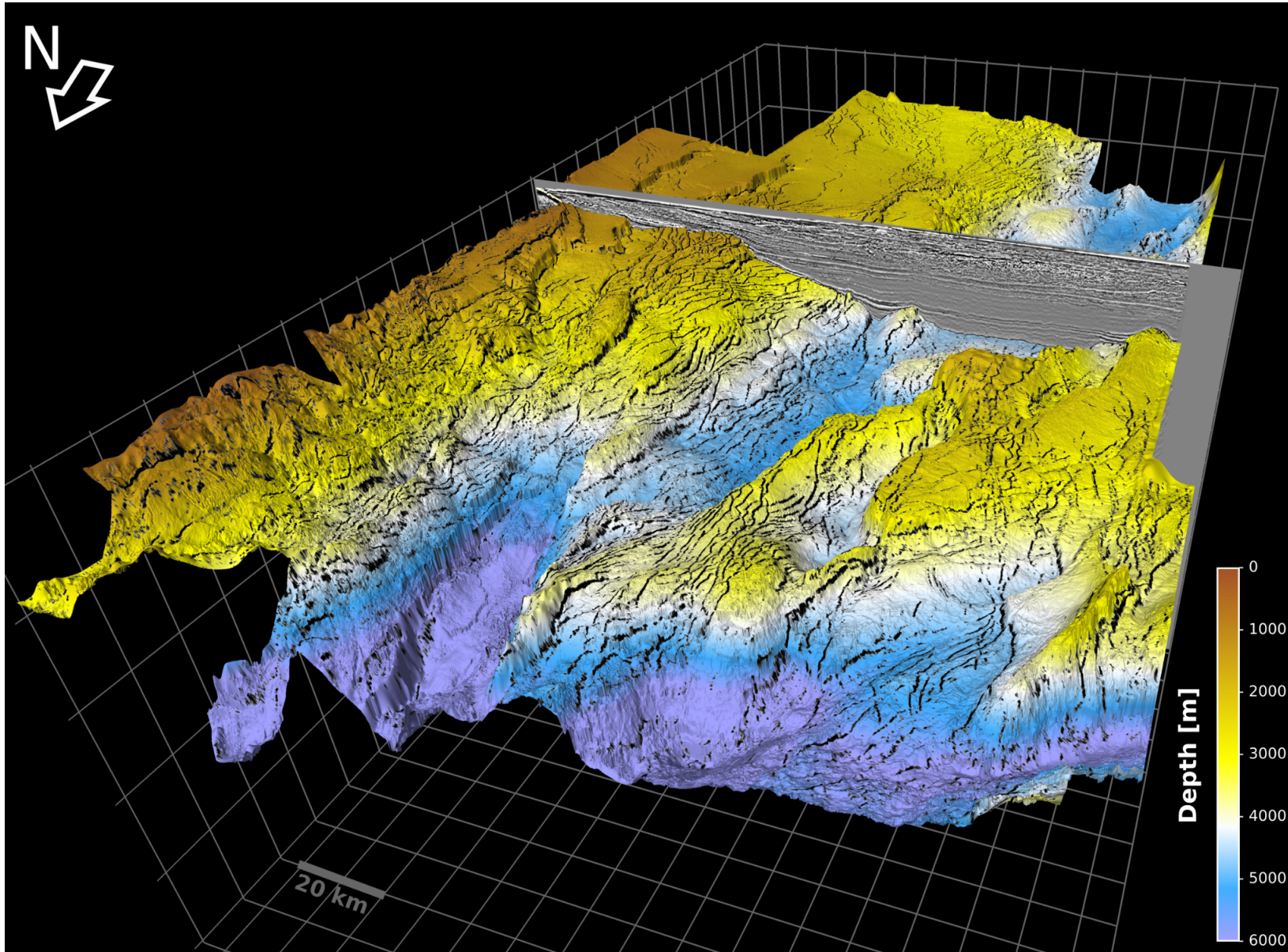


Figure 11: 3-D perspective of the northern North Sea rift showing the Base Cretaceous Unconformity overlain with faults (black) extracted from 3-D seismic reflection data with deep learning. Vertical exaggeration of 5.

245 4. OBSERVATIONS

246 Our fault extraction allows us to map a complex network consisting of 7983 individual faults
247 across an approximately 161 km-wide and 266 km-long area, covering 35,410 km² of the northern
248 North Sea rift (Fig. 7C).

249 4.1. Fault length

250 Faults vary in length by 3 orders of magnitude - from 50 m to 75.9 km, with some of the
251 longest faults (>30 km) extending from the Stord Basin and Bjørgvin Arch in the south to the Uer and
252 Lomre Terrace in the north (Fig. 10B). In cross-section, these faults have up to several kilometres of
253 displacement and bound rotated half-graben (e.g. Whipp et al., 2014; Bell et al., 2014) (Fig. 3B,C).
254 While we observe some long (up to 20 km) faults in the Viking Graben and Tampen Spur, most faults
255 (>90%) are closely spaced (< 5 km) and relatively short (<10 km long) (Fig. 10B).

256 4.2. Fault strikes

257 In map view, we observe a complex network consisting of a large number of variably trending
258 faults that display a broad range of intersection styles (e.g., oblique, perpendicular). These faults show
259 a large range of strikes, varying from NW-SE to NE-SW (Figs. 9, 10C). The length-weighted rose
260 plot shows that most faults strike NW-SE (light blue) or NNE-SSW (light orange), with a large
261 number showing intervening strike directions (Fig. 10C). This general divide occurs between
262 predominantly NW-SE-striking faults along the eastern part of the rift and NE-SW-striking faults in
263 the central and northwestern part of the rift. This divide becomes most evident when comparing faults
264 on the Lomre Terrace (NE-SW) to the adjacent Bjørgvin Arch (NW-SE), at least at the structural level
265 of the Base Cretaceous Unconformity (Fig. 10C).

266 4.3. Fault density

267 In map view, we observe large variations in fault density 500 below the BCU (Fig. 10D). While
268 dense networks of intersecting faults result in high density areas (e.g. Lomre Terrace, Bjørgvin Arch)
269 we observe low densities in the Viking and Sogn Graben, where faults occur at greater depths (e.g.
270 Fig. 9C).

271 4.4. Vertical continuity

272 The faults extracted at different depths are variable in their vertical continuity (i.e., fault height;
273 Fig. 8). Whereas some faults, in particular in the Stord Basin, the Tampen Spur, and the Magnus
274 Basin show parallel fault traces from 1 to 10 km depth (Fig. 9A), we also observe a large number of
275 faults that occur only at shallower (1-5 km) or at greater depths (6-10 km) (Fig. 9B, C). Upon closer
276 inspection, we observe that the faults, which occur continuously between 1-10 km depth, e.g. in the
277 eastern Stord Basin and the Bjørgvin Arch, are typically large-displacement normal faults with tens of
278 kilometres spacing (e.g. Fig. 3B, C), whereas the other faults, which only occur between 6-10 km
279 depth (e.g. northwestern Stord Basin), are usually shorter and more closely spaced (a few kilometres)
280 (e.g. Fig. 9C).

281

282

283 5. DISCUSSION

284 5.1. Advantages of deep learning based fault interpretation

285 When comparing our results to conventional interpretation methods, we can ask ourselves
286 “what value does deep learning add?”. Here, we highlight the advantages of the supervised deep
287 learning-based fault interpretation workflow which we present in this study. First, we can predict
288 faults in a seismic section in a fraction of the time (5 seconds) required by expert interpreters (~10
289 minutes). These differences accumulate, in particular when interpreting such a large data set with
290 >22000 inlines. A conventional fault interpretation of such a large data set can take several months,
291 whereas a trained convolutional neural network can identify faults across the entire volume within a
292 day on a single GPU (GeForce GTX 1080 Ti). Note that this comparison does not include the time
293 required to label the training data (~2 days), train the initial model (~4 hours), fine-tune and select the
294 final model (days-months). Second, after identifying faults in seismic reflection data, they also need
295 to be mapped before we can perform the relevant fault analysis. Here we map the fault network using
296 a series of tools from computer vision and network analysis compiled in our fault analysis toolbox -
297 fatbox (Wrona et al., 2022) (Figs. 6, 7). Our automated workflow extracts the fault network in less
298 than five minutes compared to the several weeks to months that would have been required to

299 manually map the faults in this large data set. Furthermore, once extracted, we can immediately
300 conduct a number of typical fault analyses using predefined functions implemented in fatbox (Wrona
301 et al., 2022) (e.g. Fig. 10).

302 Third, conventional fault interpretations are often binary (fault vs. no fault), but deep learning delivers
303 a score ranging from 0 (no fault) to 1 (fault). ~~Although this score is no true fault probability (see~~
304 ~~discussion by Mosser and Naeini, 2022), the fault score nevertheless correlates somewhat with the~~
305 ~~visibility of faults (i.e. faults, which are well-resolved by the data, are associated with higher fault~~
306 ~~scores). This allows users to qualitatively select the faults that they want to analyze using a threshold~~
307 ~~(as done herein), which allows a subsequent analysis of how likely it is to encounter a fault at any~~
308 ~~point.~~ This ~~selection~~type of analysis is particularly useful for assessing the sealing potential of certain
309 layers for CO₂ storage and for predicting fluid flow during geothermal exploration. Fourth, seismic
310 interpreters typically focus on the largest faults, whereas our model performs the same prediction
311 across the entire data set ~~irrespective of the size of the faults encountered, and does not differentiate~~
312 ~~between faults based on their size, shape or orientation.~~ Fifth, given the same data, labels, model and
313 training, our model and results are fully reproducible, which is not the case for conventional fault
314 interpretations, where the interpreter has to make a myriad of decisions in the process of mapping a
315 fault network.

316 5.2. Complex fault system in the northern North Sea

317 Our study shows how to reveal the complex geometry of normal fault systems in 3-D seismic
318 reflection data using a combination of deep learning and automated fault extraction. We were able to
319 map an intricate network consisting of almost 8000 individual faults that cover an area approximately
320 161 km wide and 266 km long (e.g. Figs. 4, 6, 10). This fault network shows large variations in fault
321 length, strike and density, with extremely complex splays, junctions and intersections between these
322 faults (Figs. 7-11). As such, our work goes far beyond typical seismic interpretations in previous case
323 studies, which covered only a fraction of the rift (e.g. Duffy et al., 2015; Deng et al., 2017; Tillmans
324 et al., 2021), or regional studies that mapped <100 of the largest faults using primarily sparse, 2-D
325 seismic sections (e.g. Fig. 1B; Fazlikhani et al., 2017; Phillips et al., 2019).

326 5.3. Uncertainties during fault mapping

327 While there are several advantages to our approach, it is worth remembering the uncertainties
328 associated with mapping faults in seismic reflection data. First, seismic reflection data can only image
329 faults with displacement above the seismic resolution (and level of noise) of the data set. The seismic
330 resolution of our data set decreases from 15 m (vertical) and 30 m (lateral) around 3 km depth down
331 to 180 m (vertical) around 20 km depth (see Wrona et al., 2019; Tillman et al., 2021). Second, the
332 labels we use to train our model are derived from 22 interpreted seismic sections, which, like any
333 seismic interpretation, contains the expertise and biases of the interpreter (e.g. Bond et al., 2007, Bond
334 2015). Third, the convolutional neural network that we trained achieves an accuracy of 83%, implying
335 that 17% of the data is misclassified (see Wrona et al., 2021). A closer inspection reveals that 36% are
336 false positives (i.e. faults that were overlooked) and 5% are false negatives (i.e. faults that were
337 misinterpreted) (see Wrona et al., 2021). Despite these limitations, the robustness of our approach is
338 evident when considering along-strike fault continuity across a large number of different seismic lines
339 (Fig. 10, 11).

340 5.4. Future research on automated fault mapping

341 Based on our work, we can identify three related areas for future research ~~on this subject~~.
342 First, conventional neural networks predict a fault score from 0 to 1, which seems to correspond to the
343 visibility of the fault in the dataset we can use as a proxy for how likely it is to encounter a fault at a
344 point. Bayesian neural networks, on the other hand, allow the prediction of true fault probabilities
345 (e.g. Mosser et al., 2020). Predicting fault probabilities in regional seismic data sets could
346 significantly accelerate the screening for and risk assessment of potential CO₂ storage sites (see
347 Wrona and Pan, 2021). Second, in addition to predicting where faults occur, we can explore the
348 prediction of other fault properties, such as displacement, fault zone permeability or even the time
349 when they were active. This would significantly allow us to study the spatial and temporal evolution
350 of fault systems in high resolution at a regional scale. Third, while our fault extraction workflow
351 currently focuses on mapping fault networks in a series of 2-D slices or horizons, we really need

352 freely-available methods to generate 3-D fault surfaces, which allow for complex fault splays,
353 junctions and intersections, as observed here.

354 6. CONCLUSIONS

355 This study shows that the combination of deep learning and network analysis applied to 3-D
356 seismic reflection data allows us, for the first time, to map almost 8000 normal faults across the entire
357 northern North Sea rift. These faults form an intricate network with complex relationships (e.g.
358 splays, junctions, intersections) including large variations in fault length (50 m to 75.9 km) and strikes
359 (NW-SE to NE-SW). As such, this work goes far beyond previous seismic studies by providing high
360 resolution fault maps at a regional scale in a fraction of the time required by conventional
361 interpretation methods.

362 ACKNOWLEDGEMENTS

363 We would like to thank The Norwegian Academy of Science and Letters (VISTA), The
364 University of Bergen and The Initiative and Networking Fund of the Helmholtz Association through
365 the project “Advanced Earth System Modelling Capacity (ESM), The Geo.X Network and Deutsche
366 Forschungsgemeinschaft (Projektnummer 460760884) for supporting this research. ~~S. Brune has been
367 funded through the Helmholtz Young Investigators Group CRYSTALS (VH-NG-1132).~~ I. Pan
368 acknowledges the NUAcT fellowship for partially supporting the work. We are grateful to CGG, in
369 particular Stein Åsheim and Jaswinder Mann, for the permission to present this data and publish this
370 work. We thank Schlumberger for providing the software Petrel 2019© and Leo Zijerveld for IT
371 support.

372

373 REFERENCES

- 374 Bartholomew, I.D., Peters, J.M., and Powell, C.M., 1993, Regional structural evolution of the North
375 Sea: Oblique slip and the reactivation of basement lineaments, *in* Petroleum Geology
376 Conference Proceedings, v. 4, p. 1109–1122, doi:10.1144/0041109.
377 Bell, R.E., Jackson, C.A.L., Whipp, P.S., and Clements, B., 2014, Strain migration during multiphase
378 extension: Observations from the northern North Sea: Tectonics, v. 33, p. 1936–1963,
379 doi:10.1002/2014TC003551.
380 Bissell, R.C., Vasco, D.W., Atbi, M., Hamdani, M., Okwelegbe, M., and Goldwater, M.H., 2011, A
381 full field simulation of the In Salah gas production and CO2 storage project using a coupled

382 geo-mechanical and thermal fluid flow simulator: *Energy Procedia*, v. 4, p. 3290–3297.
383 Bond, C.E., 2015, Uncertainty in structural interpretation: Lessons to be learnt: *Journal of Structural*
384 *Geology*, v. 74, p. 185–200, doi:10.1016/j.jsg.2015.03.003.
385 Brun, J.P., and Tron, V., 1993, Development of the North Viking Graben: inferences from laboratory
386 modelling: *Sedimentary Geology*, v. 86, p. 31–51, doi:10.1016/0037-0738(93)90132-O.
387 Chopra, S., and Marfurt, K.J., 2007, Seismic Attributes for Prospect Identification and Reservoir
388 Characterization: Society of Exploration Geophysicists and European Association of
389 Geoscientists and Engineers, doi:10.1190/1.9781560801900.
390 Claringbould, J.S., Bell, R.E., Jackson, C.A.L., Gawthorpe, R.L., and Odinsen, T., 2020, Pre-breakup
391 Extension in the Northern North Sea Defined by Complex Strain Partitioning and
392 Heterogeneous Extension Rates: *Tectonics*, v. 39, doi:10.1029/2019TC005924.
393 Clerc, C., Jolivet, L., and Ringenbach, J.C., 2015, Ductile extensional shear zones in the lower crust
394 of a passive margin: *Earth and Planetary Science Letters*, v. 431, p. 1–7,
395 doi:10.1016/j.epsl.2015.08.038.
396 Deng, C., Fossen, H., Gawthorpe, R.L., Rotevatn, A., Jackson, C.A.L., and FazliKhani, H., 2017,
397 Influence of fault reactivation during multiphase rifting: The Oseberg area, northern North
398 Sea rift: *Marine and Petroleum Geology*, v. 86, p. 1252–1272,
399 doi:10.1016/J.MARPETGEO.2017.07.025.
400 Doré, A.G., Lundin, E.R., Fichler, C., and Olesen, O., 1997, Patterns of basement structure and
401 reactivation along the NE Atlantic margin: *Journal of the Geological Society*, v. 154, p. 85–
402 92, doi:10.1144/gsjgs.154.1.0085.
403 Duffy, O.B., Bell, R.E., Jackson, C.A.L., Gawthorpe, R.L., and Whipp, P.S., 2015, Fault growth and
404 interactions in a multiphase rift fault network: Horda Platform, Norwegian North Sea: *Journal*
405 *of Structural Geology*, v. 80, p. 99–119, doi:10.1016/J.JSG.2015.08.015.
406 Færseth, R.B., 1996, Interaction of permo-triassic and jurassic extensional fault-blocks during the
407 development of the northern North Sea: *Journal of the Geological Society*, v. 153, p. 931–
408 944, doi:10.1144/gsjgs.153.6.0931.
409 Færseth, R.B., Knudsen, B.E., Liljedahl, T., Midbøe, P.S., and Søderstrøm, B., 1997, Oblique rifting
410 and sequential faulting in the Jurassic development of the northern North Sea: *Journal of*
411 *Structural Geology*, v. 19, p. 1285–1302, doi:10.1016/s0191-8141(97)00045-x.
412 FazliKhani, H., Fossen, H., Gawthorpe, R.L., Faleide, J.I., and Bell, R.E., 2017, Basement structure
413 and its influence on the structural configuration of the northern North Sea rift: *Tectonics*, v.
414 36, p. 1151–1177, doi:10.1002/2017TC004514.
415 Guo, Z., and Hall, R.W., 1992, Fast fully parallel thinning algorithms: *CVGIP: Image Understanding*,
416 v. 55, p. 317–328, doi:10.1016/1049-9660(92)90029-3.
417 Kampman, N., Bickle, M., Wigley, M., and Dubacq, B., 2014, Fluid flow and CO₂–fluid–mineral
418 interactions during CO₂-storage in sedimentary basins: *Chemical Geology*, v. 369, p. 22–50.
419 Lohr, T., Krawczyk, C.M., Oncken, O., and Tanner, D.C., 2008, Evolution of a fault surface from 3D
420 attribute analysis and displacement measurements: *Journal of Structural Geology*, v. 30, p.
421 690–700, doi:10.1016/j.jsg.2008.02.009.
422 Maystrenko, Y.P., Olesen, O., Ebbing, J., and Nasuti, A., 2017, Deep structure of the northern north
423 sea and southwestern Norway based on 3D density and magnetic modelling: *Norsk Geologisk*
424 *Tidsskrift*, v. 97, p. 169–210, doi:10.17850/njg97-3-01.
425 Moeck, I., Kwiatek, G., and Zimmermann, G., 2009, Slip tendency analysis, fault reactivation
426 potential and induced seismicity in a deep geothermal reservoir: *Journal of Structural*
427 *Geology*, v. 31, p. 1174–1182.
428 Morris, A., Ferrill, D.A., and Henderson, D.B., 1996, Slip-tendency analysis and fault reactivation:
429 *Geology*, v. 24, p. 275–278.
430 Mosser, L., Purves, S., and Naeni, E.Z., 2020, Deep bayesian neural networks for fault identification
431 and uncertainty quantification: 1st EAGE Digitalization Conference and Exhibition,
432 doi:10.3997/2214-4609.202032036.
433 Mosser, L., and Naeni, E.Z., 2022, A comprehensive study of calibration and uncertainty
434 quantification for Bayesian convolutional neural networks — An application to seismic data,
435 *GEOPHYSICS 87: IM157-IM176*. <https://doi.org/10.1190/geo2021-0318.1>
436

437 Naliboff, J.B., Glerum, A., Brune, S., Péron-Pinvidic, G., and Wrona, T., 2020, Development of 3D
438 rift heterogeneity through fault network evolution: *Geophysical Research Letters*,
439 doi:10.1029/2019gl086611.

440 Osagiede, E.E., Rotevatn, A., Gawthorpe, R., Kristensen, T.B., Jackson, C.A., and Marsh, N., 2020,
441 Pre-existing intra-basement shear zones influence growth and geometry of non-colinear
442 normal faults, western Utsira High–Heimdal Terrace, North Sea: *Journal of Structural*
443 *Geology*, v. 130, p. 103908.

444 Pan, S., Naliboff, J., Bell, R.E., and Jackson, C., 2021, Bridging spatiotemporal scales of normal fault
445 growth using numerical models of continental extension: *EarthArXiv*,
446 doi:10.31223/X5DG7M.

447 Phillips, T.B., Fazlikhani, H., Gawthorpe, R.L., Fossen, H., Jackson, C.A.L., Bell, R.E., Faleide, J.I.,
448 and Rotevatn, A., 2019, The Influence of Structural Inheritance and Multiphase Extension on
449 Rift Development, the Northern North Sea: *Tectonics*, v. 38, p. 4099–4126,
450 doi:10.1029/2019TC005756.

451 Tillmans, F., Gawthorpe, R.L., Jackson, C.A. -L., and Rotevatn, A., 2021, Syn-rift sediment gravity
452 flow deposition on a Late Jurassic fault-terraced slope, northern North Sea: *Basin Research*,
453 v. 33, p. 1844–1879, doi:10.1111/BRE.12538.

454 Torsvik, T.H., Andersen, T.B., Eide, E.A., and Walderhaug, H.J., 1997, The age and tectonic
455 significance of dolerite dykes in western Norway: *Journal of the Geological Society*, v. 154,
456 p. 961–973, doi:10.1144/gsjgs.154.6.0961.

457 Whipp, P.S., Jackson, C.A.L., Gawthorpe, R.L., Dreyer, T., and Quinn, D., 2014, Normal fault array
458 evolution above a reactivated rift fabric; a subsurface example from the northern Horda
459 Platform, Norwegian North Sea: *Basin Research*, v. 26, p. 523–549, doi:10.1111/bre.12050.

460 Wiest, J.D., Wrona, T., Bauck, M.S., Fossen, H., Gawthorpe, R.L., Osmundsen, P.T., and Faleide, J.I.,
461 2020, From Caledonian Collapse to North Sea Rift: The Extended History of a Metamorphic
462 Core Complex: *Tectonics*, v. 39, doi:10.1029/2020TC006178.

463 Wrona, T., Brune, S., Gayrin, P., and Hake, T., 2022, Fatbox - Fault Analysis Toolbox: GFZ Data
464 Services, doi:10.5880/GFZ.2.5.2022.002.

465 Wrona, T., Magee, C., Fossen, H., Gawthorpe, R.L.L., Bell, R.E.E., Jackson, C.A.-L.A.L., and
466 Faleide, J.I.I., 2019, 3-D seismic images of an extensive igneous sill in the lower crust:
467 *Geology*, v. 47, p. 729–733, doi:10.1130/G46150.1.

468 Wrona, T., Magee, C., Jackson, C.A.L.C.A.-L.C.A.L., Huuse, M., and Taylor, K.G.K.G., 2017,
469 Kinematics of polygonal fault systems: Observations from the northern north sea: *Frontiers in*
470 *Earth Science*, v. 5, p. 101, doi:10.3389/feart.2017.00101.

471 Wrona, T., and Pan, I., 2021, Can machine learning improve carbon storage? Synergies of deep
472 learning, uncertainty quantification and intelligent process control:

473 Wrona, T., Pan, I., Bell, R.E., Gawthorpe, R.L., Fossen, H., and Brune, S., 2021a, 3D seismic
474 interpretation with deep learning: A brief introduction: *Society of Exploration Geophysicists*,
475 v. 40, p. 524–532, doi:10.1190/tle40070524.1.

476 Wrona, T., Pan, I., Bell, R.E., Gawthorpe, R.L., Fossen, H., and Brune, S., 2021b, 3-D seismic
477 interpretation with deep learning: a set of Python tutorials:, doi:10.5880/GFZ.2.5.2021.001.

478 Wu, X., Liang, L., Shi, Y., and Fomel, S., 2019, FaultSeg3D: Using synthetic data sets to train an end-
479 to-end convolutional neural network for 3D seismic fault segmentation: *GEOPHYSICS*, v.
480 84, p. IM35–IM45, doi:10.1190/geo2018-0646.1.

481 Wu, K., Otoo, E., and Suzuki, K., 2009, Optimizing two-pass connected-component labeling
482 algorithms: *Pattern Analysis and Applications*, v. 12, p. 117–135, doi:10.1007/S10044-008-
483 0109-Y.

484 Yukutake, Y., Takeda, T., and Yoshida, A., 2015, The applicability of frictional reactivation theory to
485 active faults in Japan based on slip tendency analysis: *Earth and Planetary Science Letters*, v.
486 411, p. 188–198.